Intrinsic Mechanics of 3D-Printed Porous Polymer-Derived Ceramic Metamaterials

Youjian Li [a], Vahid Karamzadeh [b], Hamidreza Yazdani Sarvestani [b], Hossein Mofatteh [a], Zhengshu Yan [a,c], Ehsan Estakhrianhaghighi [a], Michael Jakubinek [d], Behnam Ashrafi [b], Javad Gholipour [b*], Abdolhamid Akbarzadeh [a,c*]

[a] Department of Bioresource Engineering, McGill University, Montreal, QC, H9X 3V9, Canada

[b] Aerospace Manufacturing Technology Center, National Research Council Canada, Montreal, QC, H3T 2B2, Canada

[c] Department of Mechanical Engineering, McGill University, Montreal, QC, H3A 0G4, Canada

[d] Division of Emerging Technologies, National Research Council Canada, Ottawa, ON, K1A 0R6, Canada

[*] *Corresponding authors:*

Abdolhamid Akbarzadeh (hamid.akbarzadeh@mcgill.ca)

Javad Gholipour (Javad.GholipourBaradari@cnrc-nrc.gc.ca)

This PDF file contains:

Section S1. Design parameters

Tables S1-2 list the as-designed parameters of cylindrical and lattice specimens, respectively. The definitions of those parameters can be found in **Figure 2** in the main text.

Table S1. The geometric parameters of the as-designed cylindrical specimens.

Specimens	**C1**	**C2**	**C3**	**C4**
Height, h (mm)	12.7	12.7	12.7	12.7
Outer radius, r_{outer} (mm)	6.35	6.35	6.35	6.35
Wall thickness, t (mm)	0.67	1	1.43	1.86
Relative densities, $\bar{\rho}$	0.2	0.3	0.4	0.5

Table S2. The as-designed parameters of SC-BCC, SC-FDC, and SC-FCC lattices.

Lattices	**Layers**	**Total length, L (mm)**	**Strut width, t (mm)**	**Relative density, $\bar{\rho}$**
SC-BCC	3	40	1.10	10%
	3	40	1.60	20%
SC-FDC	3	40	1.40	10%
	3	40	2.02	20%
SC-FCC	3	40	1.12	10%
	3	40	1.65	20%

Section S2. Scanned images using micro-computed tomography (μCT) and related calculations

Cross-sectional images of cylindrical samples are obtained from μCT scan. In CTan, the analysis software, all the images are formatted to binary with only white and black colors. The region of interest (ROI) can be selected and changed by tuning the threshold values, thus the areas of solid, solid and pores, the whole circular cross section, the inner and outer radius can be calculated, as shown in **Figure S**1. The deviations come from differences among different layers. All the other calculated values are listed in **Tables S**3-6.

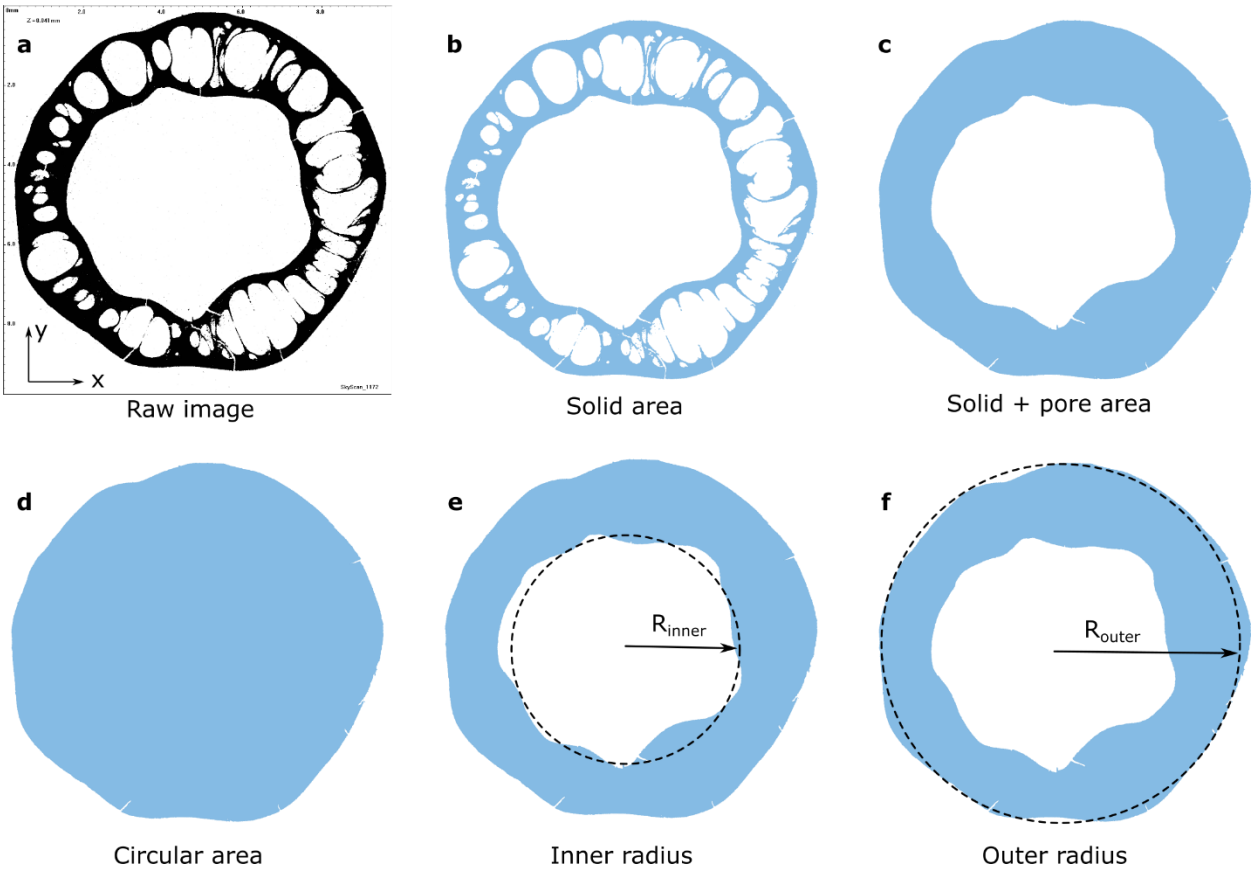

Figure S1. Schematic depiction of the calculation from **(a)** the raw μCT scan image to **(b)** solid area, **(c)** solid and pore area, **(d)** circular area, **(e)** mean inner radius, and **(f)** mean outer radius.

Table S3. Geometrical parameters of as-fabricated cylindrical specimens.

Specimens	**C1**	**C2**	**C3**	**C4**	**Average**
Bulk density (g/cm^3) *	1.63 ± 0.01	1.66 ± 0.00	1.71 ± 0.01	1.69 ± 0.00	1.67 ± 0.04
Bulk density (g/cm^3) **	1.67	1.70	1.79	1.77	1.73 ± 0.06
Porosity, φ	0.2%	1.6%	5.4%	41.4%	NA
As-designed relative density, $\bar{\rho}_d$	20%	30%	40%	50%	NA
True (as-fabricated) relative density, $\bar{\rho}_f$	24.0%	28.0%	39.3%	33.8%	NA
Height, h (mm)	6.81	7.17	7.79	7.57	NA
Solid cross-sectional area (mm^2)	13.99 ± 0.57	16.85 ± 0.68	24.27 ± 2.19	21.70 ± 1.31	NA

* Bulk density measured by gas pycnometer. ** Bulk density calculated by μCT images.

Table S4. The average, maximum, and minimum areas of the solid phase.

Samples	C1	C2	C3	C4
Average area (mm^2)	13.99 ± 0.57	16.85 ± 0.68	24.27 ± 2.19	21.70 ± 1.31
Max area (mm^2)	14.64	17.29	26.36	25.80
Min area (mm^2)	11.75	14.03	19.93	19.21

Table S5. The average, maximum, and minimum areas of the solid and pore phase.

Samples	C1	C2	C3	C4
Average area (mm^2)	14.10 ± 0.59	17.23 ± 0.48	25.40 ± 0.63	36.96 ± 3.79
Max area (mm^2)	14.85	17.70	26.62	41.67
Min area (mm^2)	11.99	14.33	24.43	26.96

Table S6. Average circular area, inner and outer radii, and wall thickness of cylindrical specimens.

Samples	C1	C2	C3	C4
Circular area (mm^2)	60.77 ± 2.56	62.97 ± 1.75	64.83 ± 1.60	68.04 ± 6.98
Inner radius (mm)	3.85 ± 0.16	3.82 ± 0.14	3.54 ± 0.12	3.15 ± 0.71
Outer radius (mm)	4.40 ± 0.09	4.48 ± 0.06	4.54 ± 0.06	4.65 ± 0.23
Wall thickness (mm)	0.54 ± 0.26	0.66 ± 0.20	1.00 ± 0.17	1.51 ± 0.95

Section S3. Experimentations on cylindrical samples

Figure S2 exhibits stress-strain curves of cylindrical samples. **Table S7** presents the experimental data from compression tests on cylindrical samples. When calculating stress, only solid cross-sectional areas are considered. Therefore, the results represent the Young's modulus of the bulk PDC material. The maximal compressive strength is determined by the ratio of maximal stress to the minimal cross-sectional area of each sample.

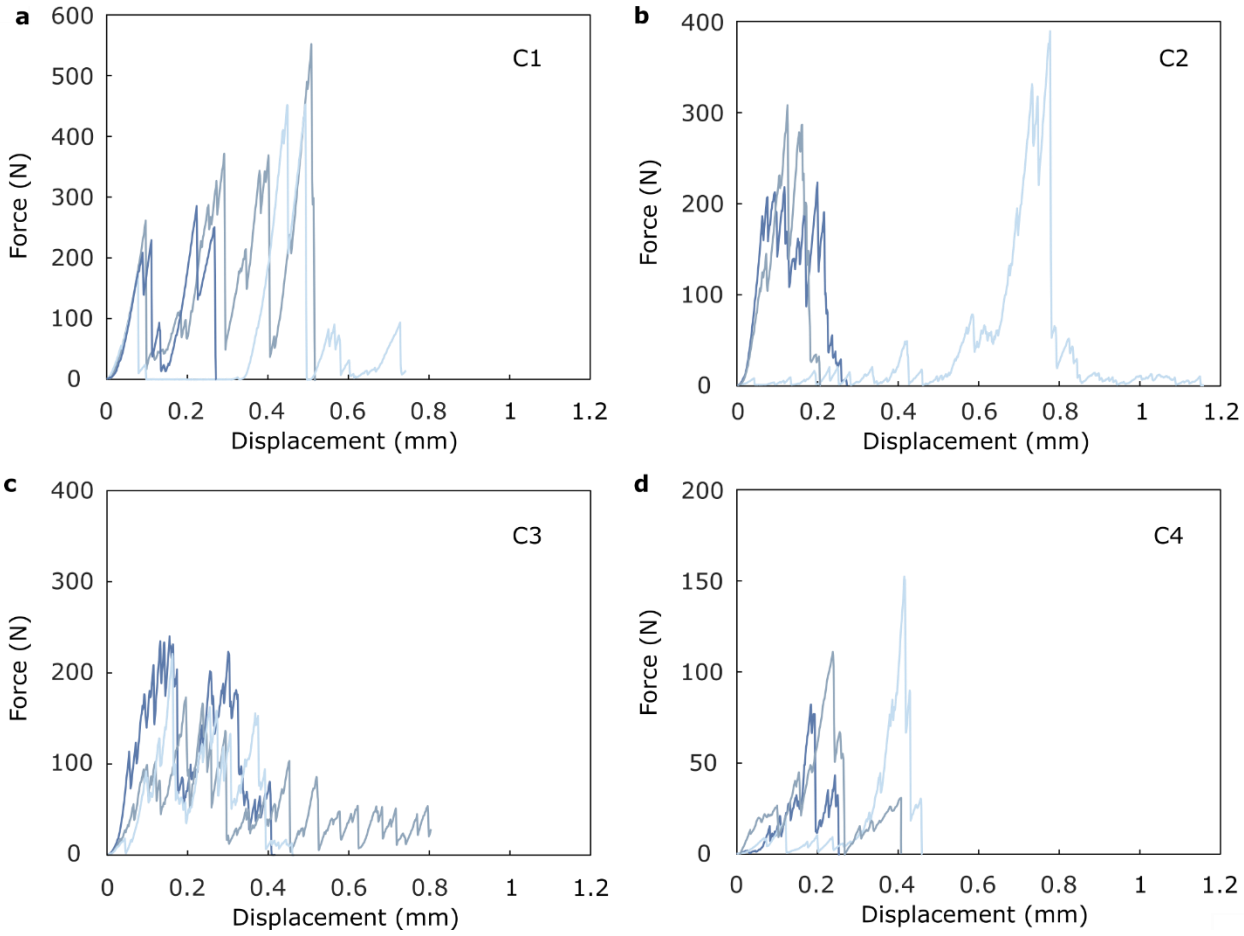

Figure S2. (a-d) Stress-strain curves of cylindrical samples.

Table S7. Compressive modulus, strength, and strain at failure of cylindrical samples.

Sample	1	2	3	4
Bulk Young's modulus (GPa)	1.91 ± 0.23	2.02 ± 0.43	1.57 ± 0.02	1.03 ± 0.41
Specific bulk Young's modulus (GPa/g·cm^3)	1.18 ± 0.14	1.21 ± 0.26	0.92 ± 0.01	0.61 ± 0.24
Maximal compressive strength (MPa)	37.61 ± 11.80	21.40 ± 5.74	10.63 ± 1.72	6.29 ± 2.59
Specific compressive strength (MPa/g·cm^3)	23.35 ± 7.32	12.21 ± 3.28	6.08 ± 0.98	3.66 ± 1.53
Strain at failure	0.015 ± 0.002	0.026± 0.006	0.021 ± 0.002	0.016 ± 0.001

Section S4. Pixel-based reconstruction

A MATLAB-based image-processing and reconstruction pipeline was developed to convert μCT images stacks into three-dimensional FE models. The workflow begins by selecting a subset of grayscale micro-CT slices at a prescribed sampling interval to balance through-thickness resolution (i.e., step number) and computational efficiency. Each slice is pre-processed and binarized to segment the solid phase from pores and voids, followed by resampling to a uniform in-plane resolution (i.e., the number of pixels) to ensure mesh regularity. The segmented slices are subsequently stacked to form a voxelized 3D representation of the specimen geometry. Based on this voxel model, a structured 3D grid is generated and discretized into eight-node hexahedral elements, with element-wise material assignment directly mapped from the binary voxel data. To mitigate reconstruction artifacts and eliminate imaging noise, 3D connectivity analysis is employed to remove isolated or unconnected regions, retaining only the largest continuous solid domain. The resulting mesh, including updated node coordinates and element connectivity, is exported for subsequent FEM simulations.

Section S5. Homogenization analysis

Supplementary to the homogenization analysis part in the main text, **Figure S3** displays the pore sizes obtained from scanned 3D-printed ceramics. These results are then used as the pore sizes in the RVEs. **Figure S4** illustrates the flow to generate an RVE that is eligible for investigating the effective mechanical properties of porous PDC. The convergence tests on the mesh element size have been done, and the results are shown in **Figure S5**. The results of Poisson's ratio are shown in **Figure S6** and **Table S8**.

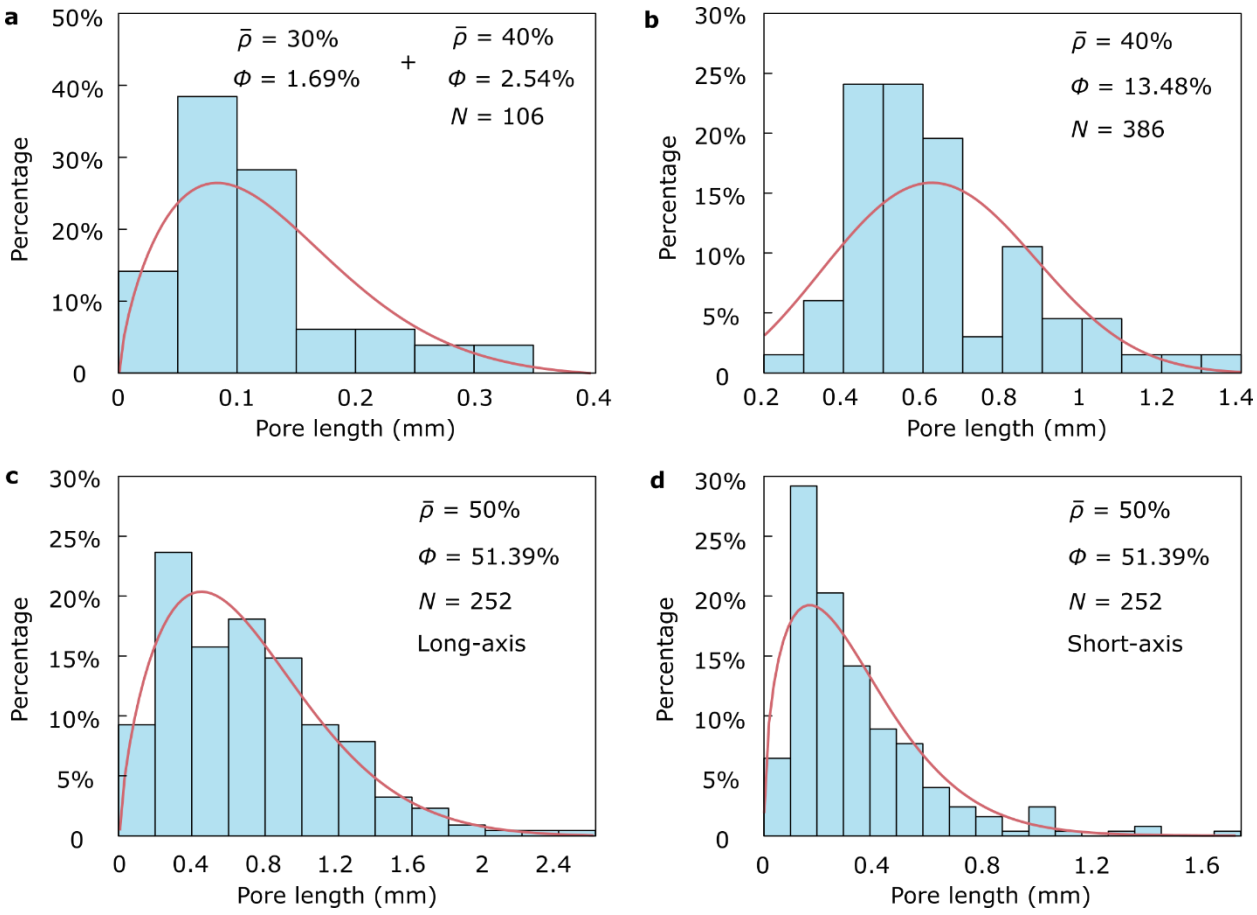

Figure S3. Dimensions of pores and their distributions.

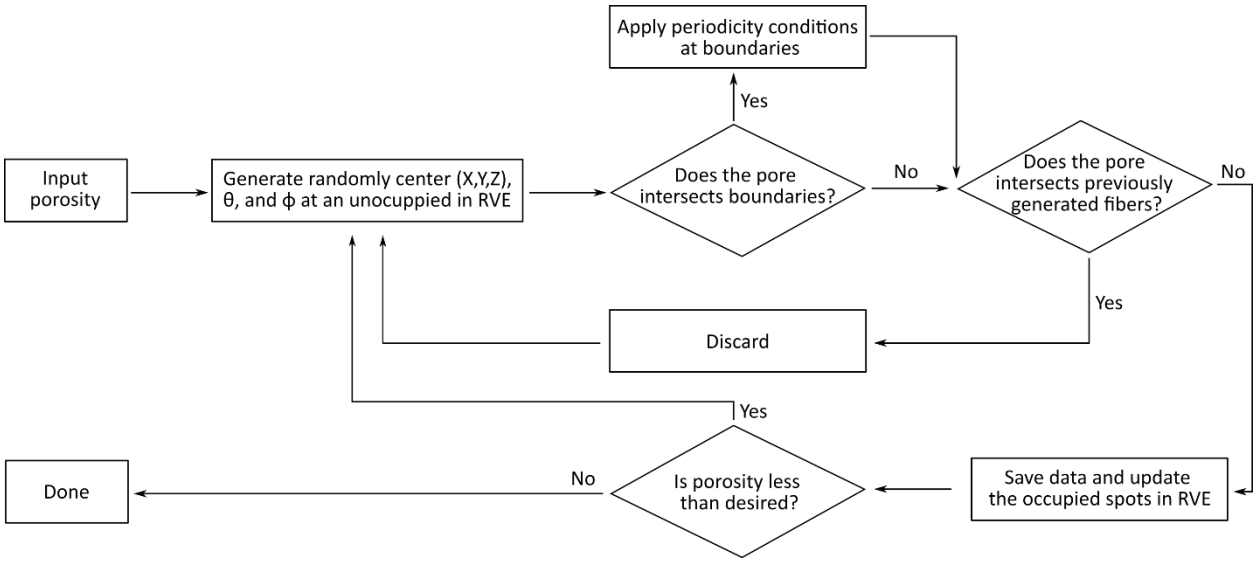

Figure S4. Modified Random sequential adsorption (RSA) flowchart.

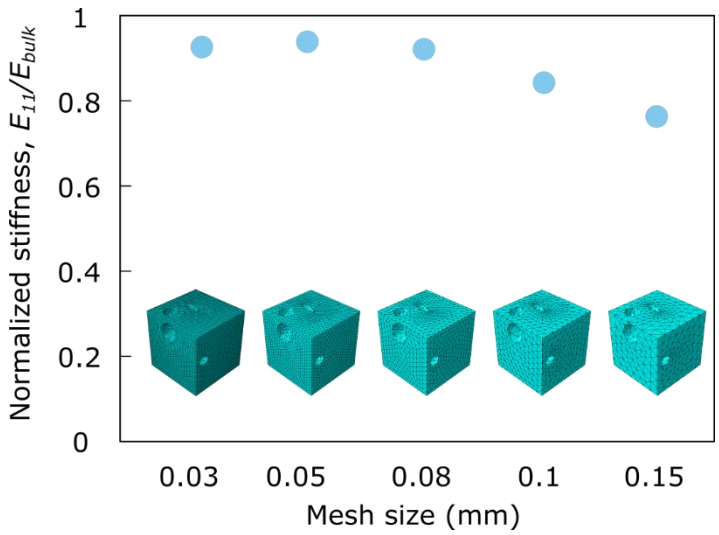

Figure S5. Results of convergence tests on the effect of mesh element size.

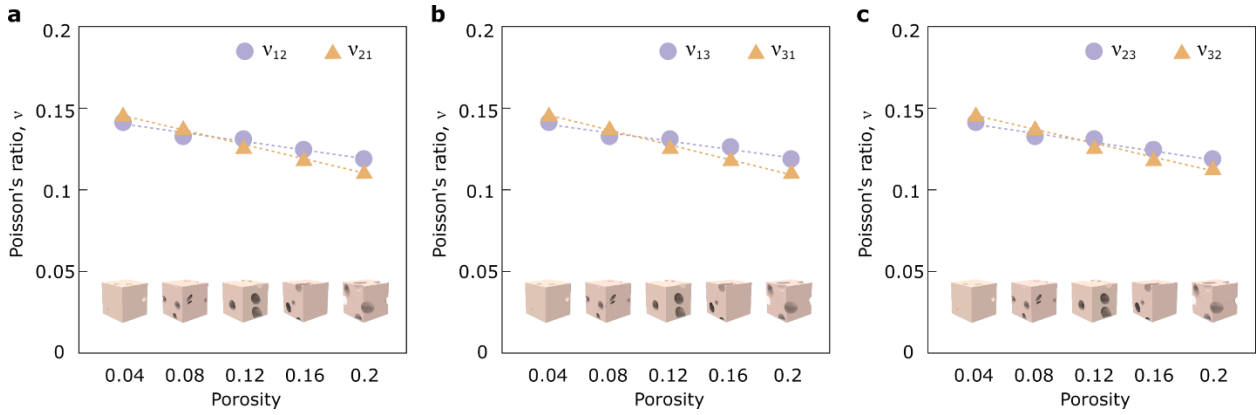

Figure S6. **(a-c)** Poisson's ratios obtained from homogenization analysis.

Table S8. Values of Poisson's ratio of RVEs with different porosities.

RVE	#1	#2	#3	#4	#5
Porosity	0.04	0.08	0.12	0.16	0.2
ν_{12}	0.3404 ± 0.0077	0.3331 ± 0.0056	0.3302 ± 0.0083	0.3237 ± 0.0088	0.3185 ± 0.0093
ν_{21}	0.3438 ± 0.0013	0.3342 ± 0.0024	0.3247 ± 0.0036	0.3169 ± 0.0080	0.3103 ± 0.0144
ν_{13}	0.3405 ± 0.0085	0.3364 ± 0.0024	0.3357 ± 0.0057	0.3312 ± 0.0074	0.3181 ± 0.0131
ν_{31}	0.3429 ± 0.0009	0.3325 ± 0.0019	0.3210 ± 0.0045	0.3181 ± 0.0055	0.3087 ± 0.0081
ν_{23}	0.3443 ± 0.0008	0.3376 ± 0.0068	0.3321 ± 0.0065	0.3240 ± 0.0038	0.3164 ± 0.0104
ν_{32}	0.3432 ± 0.0014	0.3325 ± 0.0030	0.3229 ± 0.0084	0.3178 ± 0.0024	0.3155 ± 0.0116

Section S6. Experimentations on lattices

Figures S7-8 present photos of all the as-fabricated lattice structures. Since samples with a relative density of 30% are heavily distorted and not used in experiments, SC-FCC have not been printed. **Figure S9** displays stress-strain curves from the compression tests on these lattice samples. **Table S9** presents Young's modulus of varied lattices from experiments and simulations. **Figure S10** shows how the samples under compression deform and how the fracture occurs and propagate. **Figure S11** exhibits fragments from broken samples after tests.

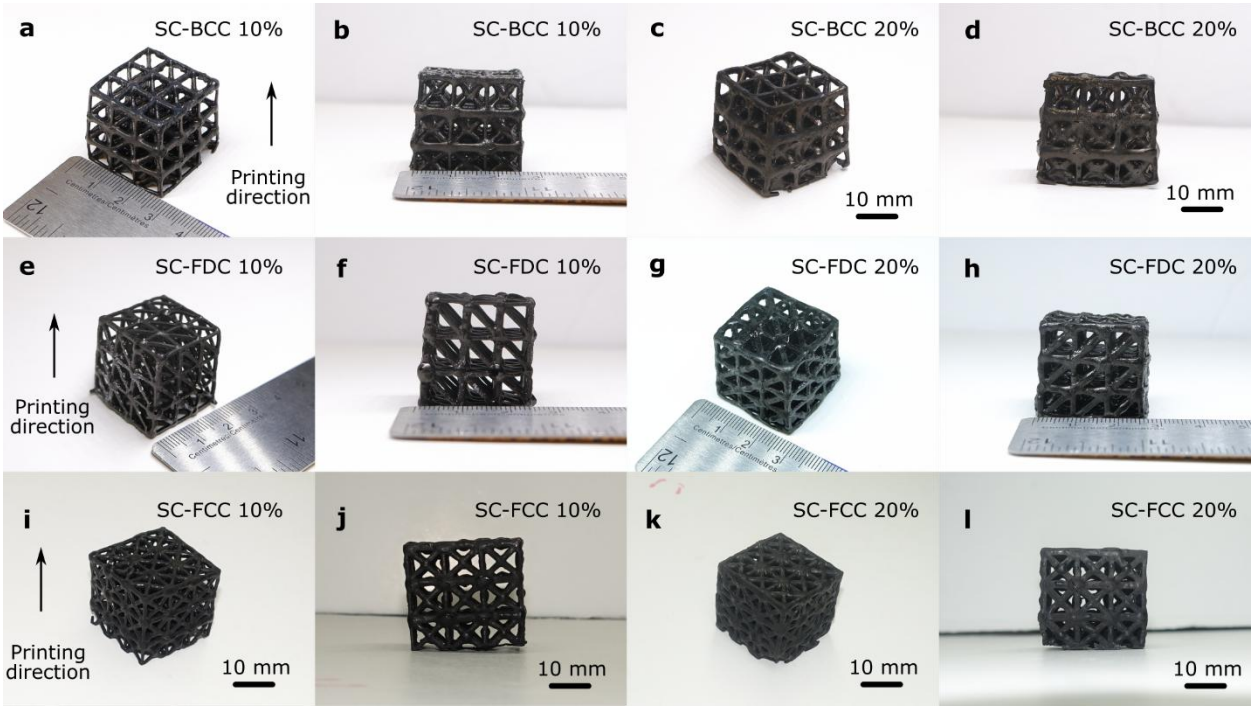

Figure S7. Photos of 3D-printed PDC-based **(a-b)** SC-BCC with a relative density of 10% and **(c-d)** 20%, **(e-f)** SC-FDC with a relative density of 10% and **(g-h)** 20%, and **(i-j)** SC-FCC with a relative density of 10% and **(k-l)** 20%. The printing direction is vertically upwards for all the samples.

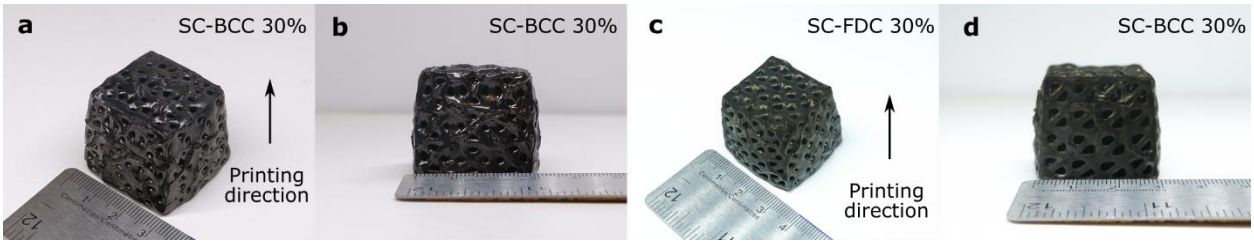

Figure S8. Photos of **(a-b)** SC-BCC with a relative density of 30%, and **(c-d)** SC-FDC with a relative density of 30%. These samples are nearly bulk. The printing direction is vertically upwards for all the samples.

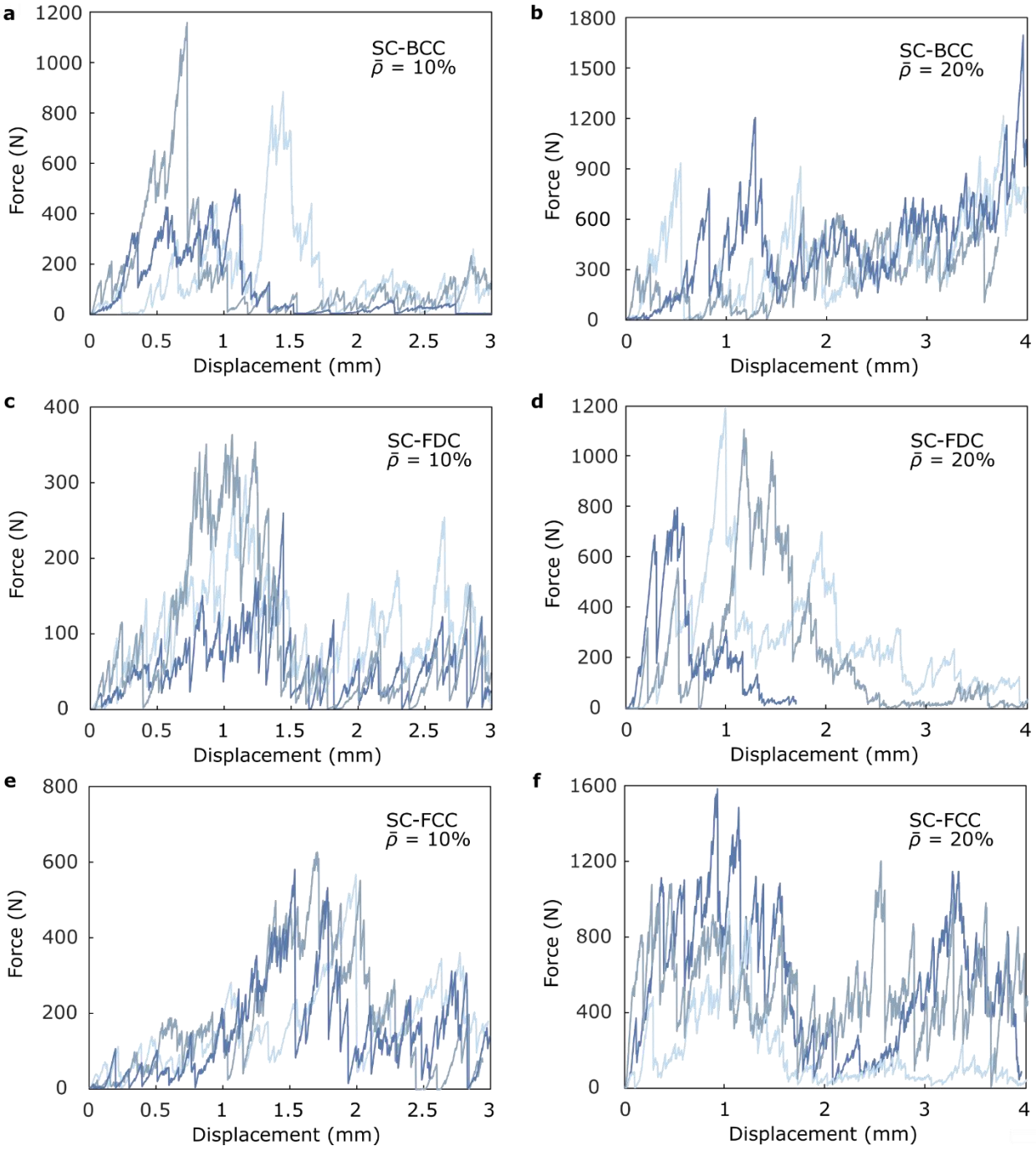

Figure S9. Stress-strain curves of **(a)** SC-BCCs with a relative density of 10% and **(b)** 20%, **(c)** SC-FDCs with a relative density of 10% and **(d)** 20%, **(e)** SC-FCCs with a relative density of 10% and **(f)** 20%.

Table S9. Numerical and experimental Young's modulus of SC-BCC, SC-FDC, and SC-FCC with relative densities of 10% and 20%, respectively.

	As-designed relative density, $\bar{\rho}_d$	Young's modulus, E (MPa)	
		FEM	Test
SC-BCC	10%	112.5	104.2 ± 15.2
	20%	145.4	152.2 ± 14.4
SC-FDC	10%	81.1	74.3 ± 4.6
	20%	139.5	165.4 ± 18.7
SC-FCC	10%	77.4	63.0 ± 6.5
	20%	123.6	137.8 ± 14.2

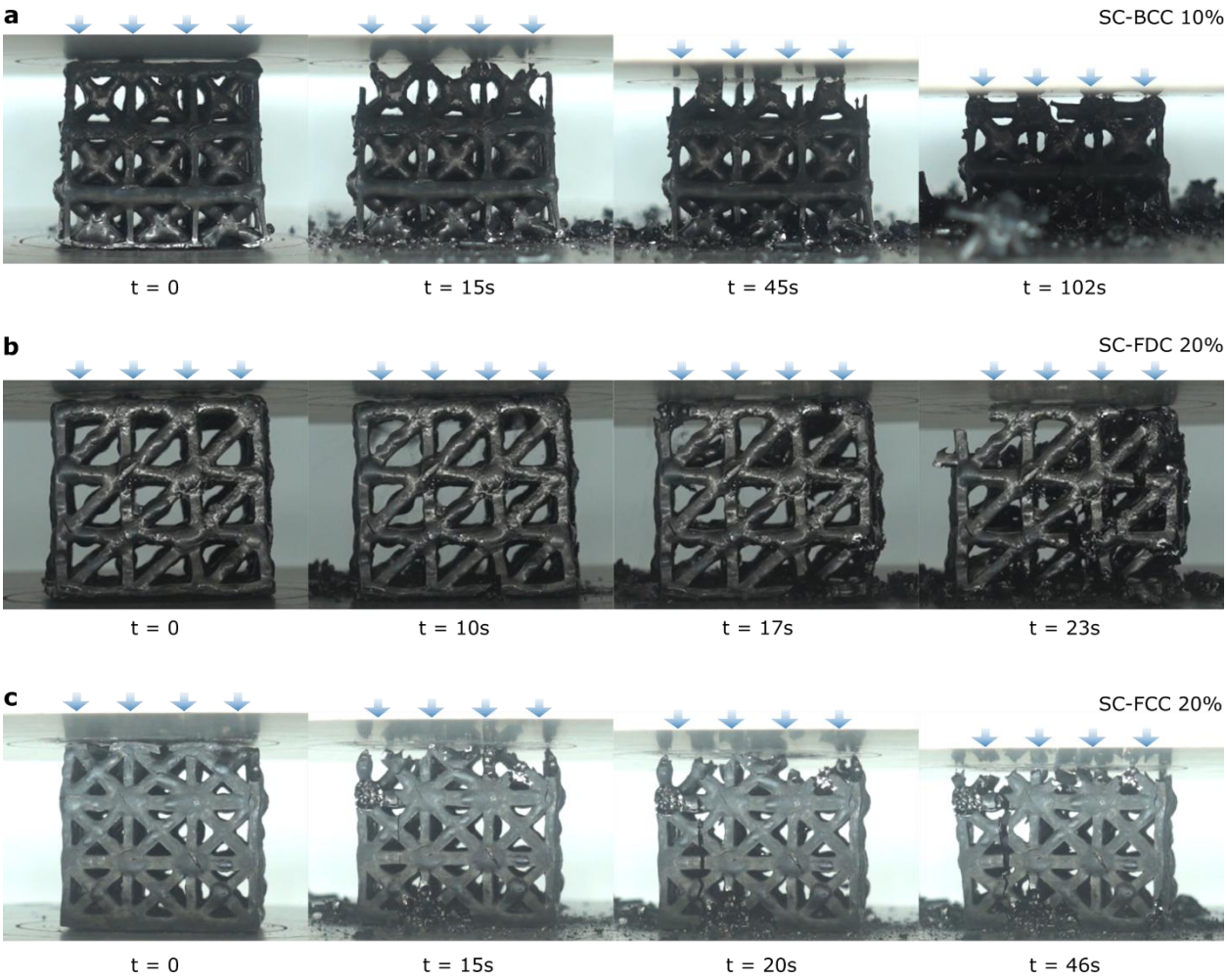

Figure S10. Screenshots from videos demonstrate **(a)** SC-BCC with a relative density of 10%, **(b)** SC-FDC with a relative density of 20%, and **(c)** SC-FCC with a relative density of 20% that are under compression.

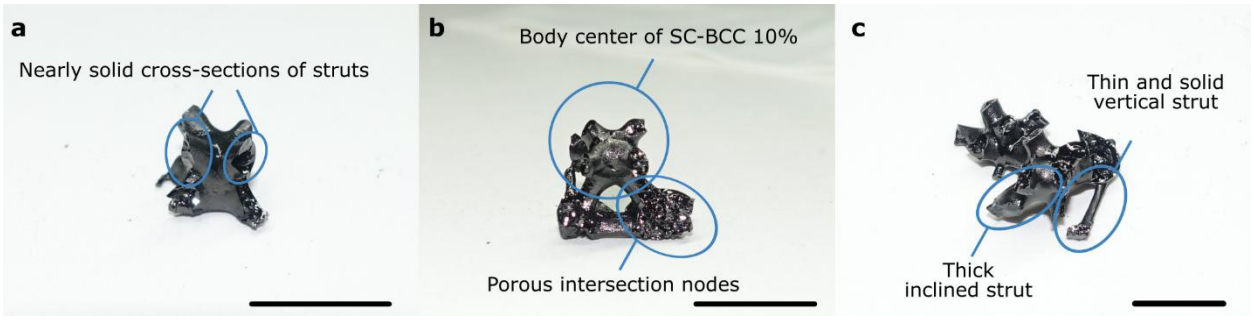

Figure S11. **(a-c)** Fragments from broken samples.

Section S7. Finite element modelling (FEM) simulations

In FEM & Homogenization, an intact lattice model with a regular geometry is employed and assigned with an effective Young's modulus obtained from **Equation 4**. The geometric parameters are determined using the average values measured from the as-fabricated samples for each case. For example, for one of the as-fabricated SC-FDC with a relative density of 10% (**Figures S7**e-f), the average length is 25.66 ± 0.16 mm; thus, the length of the intact lattice is set to 25.66 mm. The average thickness of the as-fabricated vertical struts is 0.98 mm, while that of the remainder is 1.39 mm. Based on the porosities calculated from graded SC-BCC, as summarized in **Tables S10-12**, the porosities of the vertical struts and the remaining parts of this intact geometry are estimated to be 8.7% and 39%, respectively. Based on **Equation 4**, the corresponding effective Young's moduli for these two partitions are calculated to be1688 and 676 MPa, respectively. The weighted average strut width, 1.28 mm, is adopted as the representative strut width of this geometry. All as-fabricated values are measured using a caliper. Since the ceramic is brittle and bulgy, errors cannot be avoided, and the samples are prone to fracture during measurement.

Two SC-BCC lattices were manufactured to validate the proposed strategy on structures with a larger number of unit cells. The two samples are named SC-BCC5-1 and SC-BCC5-2. They are designed to have a relative density of 20% and a total length of 40 mm. Take the sample SC-BCC5-1 as an example, the average length is measured to be 29.16 ± 1.06 mm, and thus, the length of the intact lattice is set to 29.16 mm. The average thickness of the as-fabricated vertical struts is 0.85 mm, while that of the remainder is 1.21 mm. Based on the porosities calculated from graded SC-BCC, as summarized in **Tables S10-12** (Section S7, Supplementary Information), the porosities of the vertical struts and the remaining parts of this intact geometry are estimated to be 7% and 30%, respectively. Based on **Equation 4**, the corresponding effective Young's moduli for these two partitions are calculated to be 1745 and 975 MPa, respectively. The weighted average strut width of 1.12 mm is adopted as the representative strut width of this geometry.

Figure S14 demonstrates the experimental and numerical results of SC-BCC5-1 and 5-2 lattices. The unit cells of these structures are relatively regular, while the edges are not straight due to the shrinkage. The top surfaces and corners are damaged or distorted during the manufacturing process. After conducting compression tests, the force-displacement ratio of SC-BCC5-1 is calculated to be 5.4 kN/mm, and the Young's modulus is 175.3 MPa. The results for SC-BCC5-2 are 5.0 kN/mm and 161.5 MPa. Both results show a good agreement with FEM results. For SC-BCC5-1, the

simulated force-displacement ratio and Young's modulus are 4.7 kN/mm and 159.6 MPa, respectively, while those for SC-BCC5-2 are 4.7 kN/mm and 157.8 MPa, respectively. Therefore, the effectiveness of the proposed strategy is validated by SC-BCC 5×5×5 lattices.

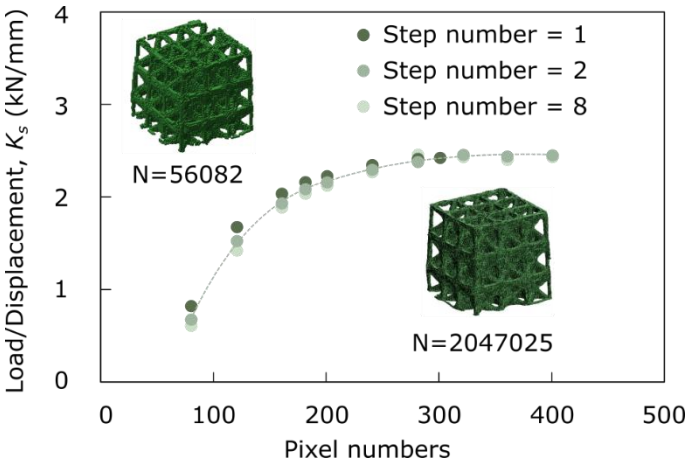

Figure S12. The effect of pixel numbers and step numbers on the reconstructed SC-BCC with a relative density of 10%. *N* represents the number of mesh elements.

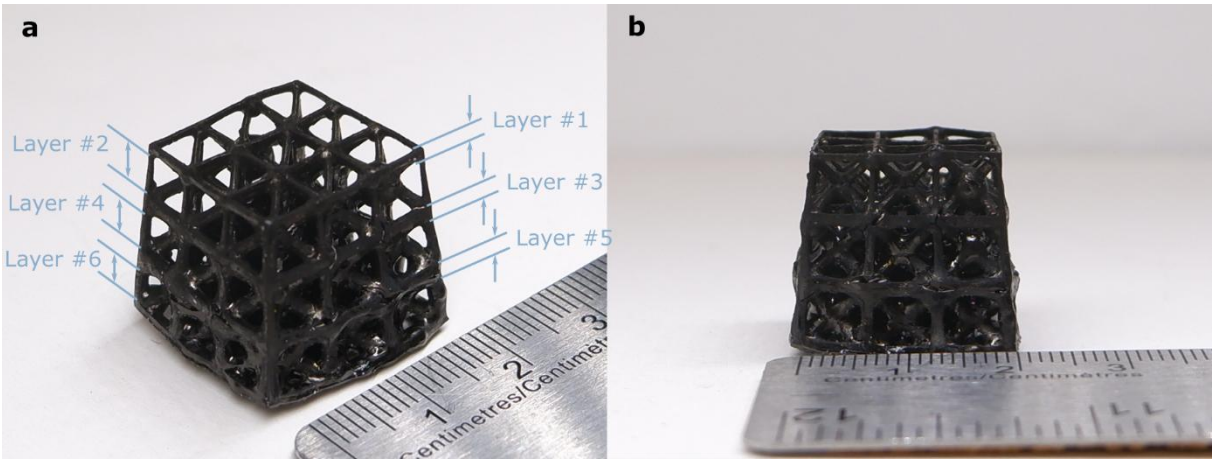

Figure S13. **(a-b)** Photos of 3D-printed graded SC-BCC lattice. Layers 1, 3, and 5 comprise only horizontal struts while Layers 2, 4, and 6 consist of vertical and inclined struts. The bottom layer, which should be Layer 7, is partially covered by the adhesive supporting rubber during the scanning process so it is not included in the calculation process.

Table S10. Porosities of each layer in 3D-printed graded SC-BCC.

Layer number	Porosity
1	15.7%
2	19.9%
3	29.1%
4	37.0%
5	37.6%
6	41.4%
Total	39.4%

Table S11. The as-designed and as-built strut width and porosities of Layer 1, 3, and 5 in graded SC-BCC.

Layer number	As-designed strut width (mm)	As-built vertical strut width (mm)	Porosity
2	0.6 - 1.07	0.47 – 0.57	0.6%
4	1.07 -1.53	0.71 – 0.90	6.8%
6	1.53 - 2	1.06 – 1.28	10.5%
		1.28 – 1.48	14.1%

Table S12. As-designed and as-built strut width and porosities of vertical struts of Layer 2, 4, and 6 in Graded SC-BCC.

Layer number	As-designed strut width (mm)	As-built strut width (in-plane) (mm)	As-built strut width (out-of-plane) (mm)	Average strut width (mm)	Porosity
1	0.6	0.43 ± 0.06	0.76 ± 0.07	0.60 ± 0.07	15.7%
3	1.07	0.71 ± 0.11	1.25 ± 0.15	0.98 ± 0.14	29.1%
5	1.53	1.14 ± 0.20	1.53 ± 0.15	1.34 ± 0.17	37.6%

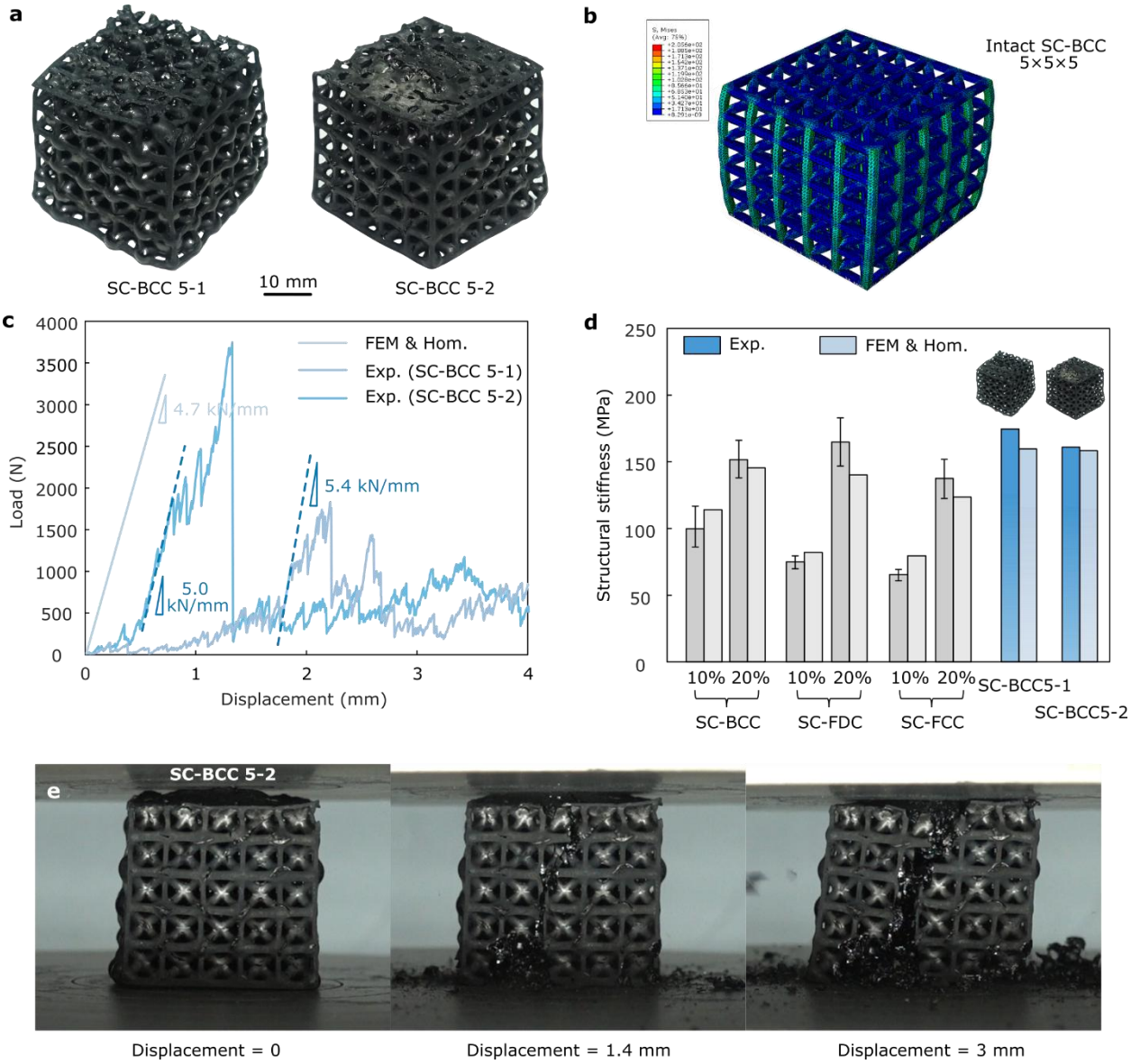

Figure S14. Experimental and simulation results of the two SC-BCC 5×5×5 structures. (a) Photos of SC-BCC 5-1 and 5-2. The unit cells of these structures are relatively regular, while the edges are not straight due to the shrinkage. The top surfaces and corners are damaged or distorted during the manufacturing process. **(b)** FEM results of the idealized SC-BCC 5×5×5 lattice. Vertical struts that are assigned with a low-porosity modulus withstand high stress upon loading. **(c)** Force-displacement curves of SC-BCC 5-1 and 5-2, compared with FEM results. A good agreement between them is demonstrated. **(d)** A bar chart exhibiting the comparison of the experimental and numerical Young's modulus of SC-BCC 5×5×5 lattices. **(e)** Screenshots showing the experimental process of SC-BCC 5-2 lattice. A major crack occurs to the middle part of the sample and causes a fracture.

Section S8. Scanning electron microscopy (SEM) on fragments

SEM was performed on a fractured fragment of 3D-printed lattices after testing. A Hitachi TM-1000 microscope was used at an accelerating voltage of 1.5 keV and a current of approximately 107 μA, noting that the current varied with magnification. The pixel size ranged from 3613.28 nm to 96.35 nm as the magnification increased from 40× to 1500×. The images were processed using ImageJ to measure the dimensions of voids.

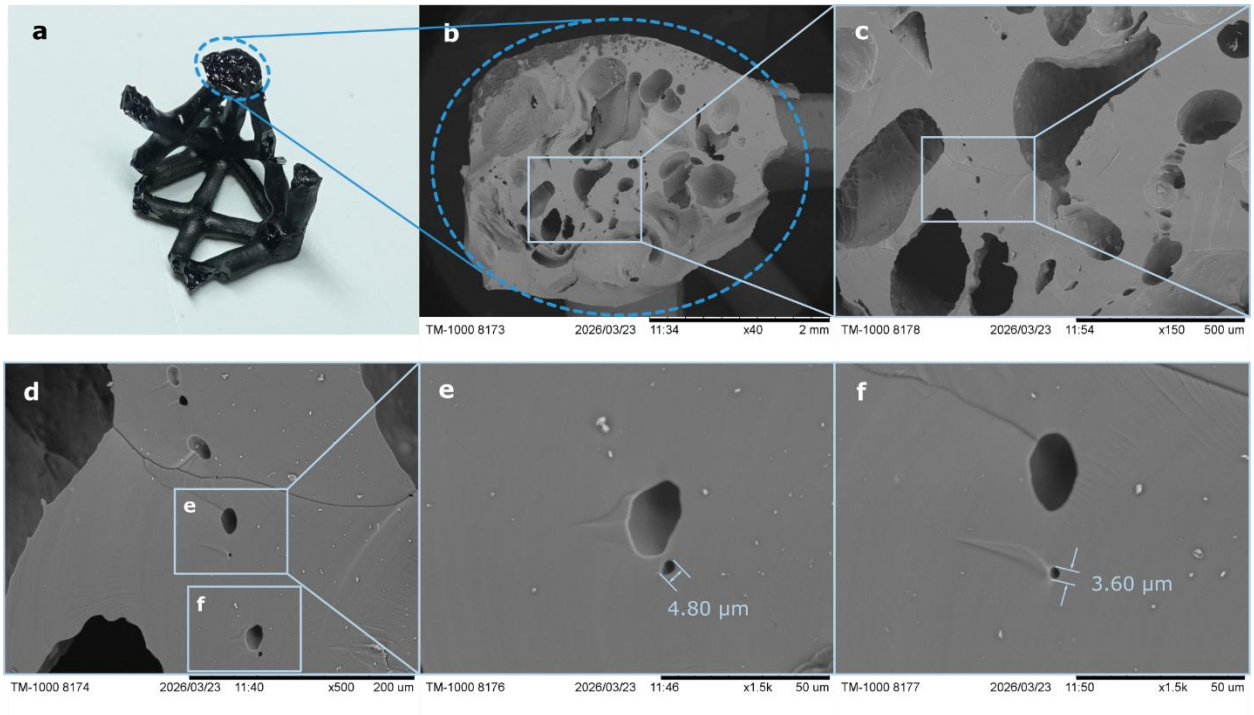

Figure S15. (a-f) SEM images on a fractured sample, showing the porosity distribution.

Since the minimum resolution of μCT is 9.89 μm, SEM was employed to investigate the presence of pores smaller than this limit, as well as their morphology and distribution, thereby providing a more complete and comprehensive assessment of the porosity in PDCs. As shown in Figures S14–S15, the number of these fine-scale voids is significantly lower than that of macro- and micro-voids. They are dispersed across the cross-section and are mainly located in solid regions far from larger pores. Their shapes are approximately ellipsoidal, similar to those of macro pores, with semi-major axes around 5 μm, while the minimum observed size is 2.68 μm. These sub-voxel voids are commonly observed alongside micro-pores with lengths ranging from 10 to 100 μm. However, Figure S15c does not show any sub-voxel voids in such regions, suggesting that their occurrence is limited.

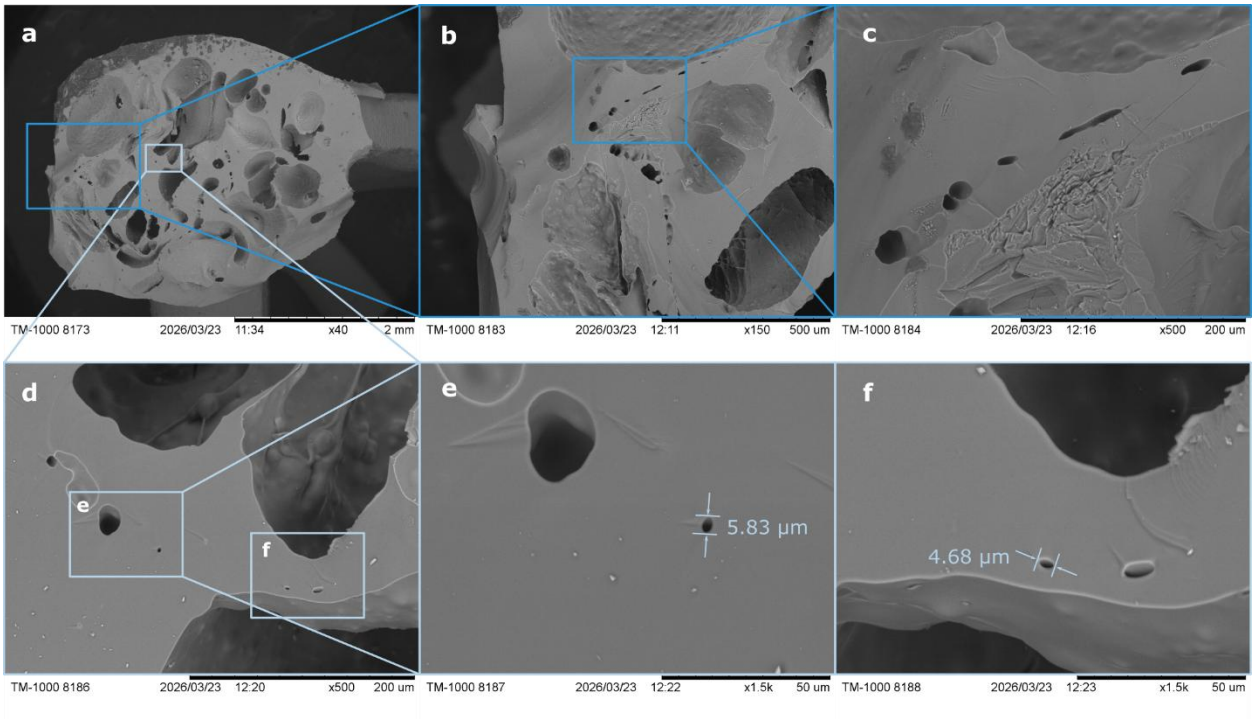

Figure S16. (a-f) SEM images on a fractured sample, showing the porosity distribution in a different region from Figure S14.